Nano Research 2018, 11(4): 2285–2294
https://doi.org/10.1007/s12274-017-1850-6
Research Article
ISSN 1998-0124
CN 11-5974/O4

Doxorubicin-loaded silicon nanoparticles impregnated into red blood cells featuring bright fluorescence, strong photostability, and lengthened blood residency

Airui Jiang[§], Bin Song[§], Xiaoyuan Ji, Fei Peng, Houyu Wang, Yuanyuan Su, and Yao He (✉)

Laboratory of Nanoscale Biochemical Analysis, Jiangsu Key Laboratory for Carbon-Based Functional Materials and Devices, Institute of Functional Nano & Soft Materials (FUNSOM), and Collaborative Innovation Center of Suzhou Nano Science and Technology (NANO-CIC), Soochow University, Suzhou 215123, China

[§] *Airui Jiang and Bin Song contributed equally to this work.*

Received: 7 July 2017
Revised: 10 September 2017
Accepted: 11 September 2017

KEYWORDS
fluorescent silicon nanoparticles,
multi-function,
red blood cells,
drug delivery system

ABSTRACT

Based on the unique advantages of fluorescent silicon nanoparticles (SiNPs), long circulation red blood cells (RBCs), and anti-cancer drug molecules (i.e., doxorubicin (DOX)), we developed multifunctional DOX-loaded SiNPs impregnated into RBCs. Importantly, the resulting drug delivery systems (DDSs) simultaneously exhibited bright fluorescence coupled with robust photostability (i.e., ~ 24% loss of fluorescent intensity after 25 min continuous laser irradiation) and significantly lengthened blood residency (i.e., $t_{1/2}$ = 7.31 ± 0.96 h, 3.9-fold longer than pure DOX-loaded SiNPs). Therefore, this novel DDS featuring multi-functionalities shows high potential for cancer diagnosis and therapy, particularly for tumor imaging and chemotherapy in a synchronous manner.

1 Introduction

In the last decade, drug delivery systems (DDSs) with attractive cancer cure rates have been extensively studied [1–5]. A recent exciting category in biomimetic nano-engineering is the cell-based DDS [3–5], such as white blood cell membrane-decorated silica particles [6], cancer cell membrane-cloaked poly(lactic-co-glycolic acid) nanoparticles (PLGA NPs) [7], bacterial membrane-coated gold NPs [8], and PLGA NPs biointerfaced by platelet membrane cloaking [9]. Among these, red blood cells (RBCs) have unique advantages, such as high drug loading capacity and slow drug diffusion properties, inherent biocompatibility, and extended lifespan [10–13]. RBC-based DDSs, including but not limited to cargo-loaded RBCs, natural RBCs-mimicking synthetic delivery vehicles, RBC membrane-derived liposomes, and RBC membrane-camouflaged NPs, are currently undergoing preclinical or clinical development [14, 15]. For example, using natural RBCs, Zhang et al.

Address correspondence to yaohe@suda.edu.cn

developed a novel "top-down" approach to tailor the RBC membrane into the nanometer range and encapsulate core PLGA NPs for increased blood circulation time [16, 17]. Using the same strategy, Ma et al. demonstrated a unique RBC membrane-derived DDS in which chemotherapeutic drugs (paclitaxel and doxorubicin (DOX)) and Fe_3O_4 nanocrystals can be co-encapsulated into O-carboxymethyl-chitosan NPs. Particularly, Arg-Gly-Asp anchored RBC membrane can act as a natural camouflage to improve the circulation time and tumor accumulation of multi-functional nanocarriers [18]. While these achievements allow NPs to be viewed as "self" and extend their half-life significantly, most established RBC-based DDSs are non-fluorescent, limiting the long-term and real-time imaging of drug transport and release process and thus hindering the comprehensive understanding of intracellular behavior of drug carriers [19, 20]. Alternatively, fluorescent organic dyes and II–VI quantum dots with intrinsic fluorescence have been encapsulated in RBCs [21, 22], which can overcome the above non-fluorescent issue to some extent. The photobleaching limitation of organic dyes and potential toxicity concerns of II–VI quantum dots have created an urgent demand for new types of RBC-based biocompatible and photostable fluorescent drug carriers.

Silicon nanomaterials have been widely studied because of their excellent optical/electronic/mechanical properties, surface tailorability, and rich abundance, among other factors [23–27]. Particularly, fluorescent silicon nanoparticles (SiNPs) have attracted broad attention because of their excellent optical properties and non- or low toxicity [28–31]. In recent years, great advancements have led to the development of biocompatible and photostable SiNPs with strong fluorescence (photoluminescence quantum yield values generally range between 30%–50%, and can reach as high as 90% under optimum conditions [28–30, 32, 33]). Based on this, we recently loaded DOX molecules onto fluorescent SiNPs to construct drug nanocarriers, illustrating a proof-of-concept for chemotherapy [34]. However, the ultrasmall size of DOX-loaded SiNPs (diameter: ~ 4 nm) often leads to rapid excretion by renal clearance and short blood half-life, limiting their widespread bioapplication [35]. Consequently, fluorescent and biocompatible DDSs capable of long-term cellular tracking and prolonged blood retention time are needed.

To overcome these critical issues, in this study, we developed DOX-loaded SiNPs impregnated into RBCs (SiNPs-DOX@RBCs). Importantly, the fluorescent SiNPs-DOX@RBCs showed favorable biocompatibility (e.g., maintained ~ 90% cell viability at 0.6 μg·mL^{-1} DOX) and strong photostability (~ 24% loss of intensity after 25 min continual laser irradiation; in comparison, the fluorescence of free DOX is rapidly quenched in 3 min under the same experimental conditions). In addition to the superior optical properties, the blood circulation time of the SiNPs-DOX@RBCs was significantly lengthened to 7.3 h under optimal conditions, which is in sharp contrast to the short-level circulation time of pure SiNPs-DOX (1.9 h).

2 Experimental

2.1 Preparation of the SiNPs-DOX@RBCs

Highly fluorescent and water-dispersible SiNPs are firstly prepared via our reported synthetic approach (please see detailed information in the Electronic Supplementary Material (ESM)) [32]. SiNPs-DOX were prepared as previously described (detailed information is presented in the ESM) [34]. Thereafter, the prepared SiNPs were loaded with DOX molecules via a simple one-step procedure, in which DOX molecules are loaded onto SiNPs via hydrophobic interactions between DOX and SiNPs and weak interactions between DOX molecules, producing the SiNPs-DOX complex [34, 36, 37]. To fabricate SiNPs-DOX@RBCs, we use an established dilutional hypotonic hemolysis method to enable the encapsulation of SiNPs-DOX by RBCs. [38, 39], as shown in Fig. 1. Briefly, whole blood was collected from the orbital sinus of Balb/c mice. RBCs were separated from whole blood by centrifugation (900*g*, 5 min) and washed twice with cold phosphate buffer saline (PBS). Next, 100 μL of packed RBCs were re-suspended in cold 0.5× hypotonic PBS (5 mM $NaHCO_3$, 5 mM NaH_2PO_4, 10 mM glucose, 2 mM $MgCl_2$), 2 × 10^{-3} M ATP, and 3 × 10^{-3} M glutathione (GSH) including SiNPs-DOX (containing 35 μg·mL^{-1} DOX) and incubated at 4 ℃ for 45 min with stirring in a hypotonic buffer. Subsequently, the isotonicity was

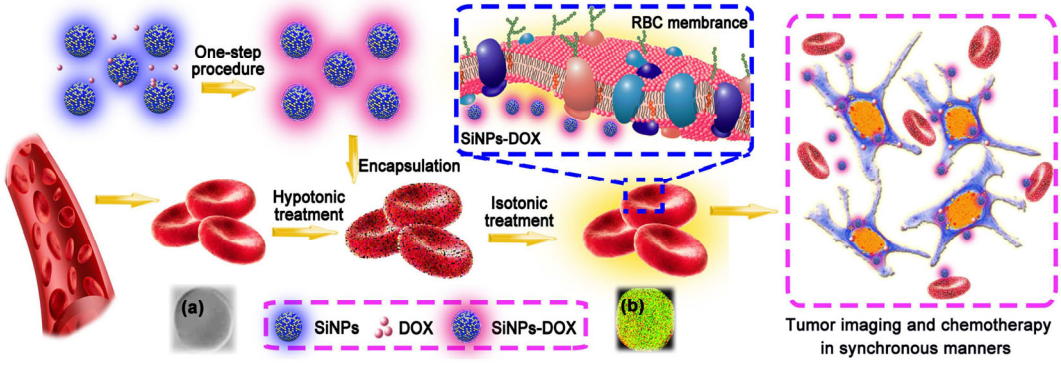

Figure 1 Schematic illustration of fabrication of SiNPs-DOX@RBCs for tumor imaging and chemotherapy. The CLSM images at the bottom present a single SiNPs-DOX@RBC in bright field (a) and fluorescent tunnel (b).

reconstituted by adding hypertonic PBS containing 10% PIGPA-NaCl (5 mM adenine, 100 mM inosine, 100 mM sodium pyruvate, 3.5×10^{-2} M NaH_2PO_4, 100 mM glucose with 12% NaCl), 2×10^{-3} M ATP, and 3×10^{-3} M GSH at 37 ˚C for 0.5 h. Osmotic pressure was reconstituted to encapsulate the SiNPs-DOX into RBCs. The resealed RBCs were washed twice with ice-cold PBS (1,500 rpm, 5 min).

2.2 Quantification of SiNPs-DOX inside RBCs

The amount of SiNPs-DOX encapsulated inside the RBCs could not be accurately estimated by ultraviolet–visible (UV–vis) spectroscopy because of the interference of hemoglobin absorption. Therefore, SiNPs-DOX@RBCs were treated with lysis buffer and then SiNPs-DOX were extracted from the cell lysis buffer by HCl/isopropanol solvent. SiNPs-DOX released from SiNPs-DOX@RBCs was collected by centrifugation at 3,000 rpm for 5 min. The fluorescence of released SiNPs-DOX in the supernatant was used to determine SiNPs-DOX release from the RBCs.

2.3 Photostability assessment of SiNPs-DOX@RBCs

Human U87MG glioblastoma cancer cells (U87MG cells) were treated with SiNPs-DOX@RBCs for 24 h before imaging. U87MG cells were used because glioblastoma is an aggressive cancer, and the prognosis for glioblastoma patients remains poor [40]. Samples were observed using a confocal laser scanning microscope (CLSM). SiNPs and DOX were excited by 50% power of the diode laser ($\lambda_{excitation}$ = 405 nm) and 20% power of the argon laser ($\lambda_{excitation}$ = 488 nm), respectively. The emission windows of SiNPs and DOX were 420–500 nm and 550–620 nm, respectively. The offset was set to −2% to ensure that no cell fluorescence background was detected. The samples were continuously laser-irradiated, and images were captured at predetermined intervals. All images were captured and processed using image analysis software.

2.4 Drug delivery behavior of SiNPs-DOX@RBCs

To evaluate the *in vitro* drug delivery behavior of the SiNPs-DOX@RBCs, U87MG cells were first cultured at 37 ˚C for 24 h under 5% CO_2 in 24-well plates at 1×10^5 cells/well, and then co-incubated with SiNPs-DOX@RBCs (containing 2.5 μg·mL^{-1} DOX) at 37 ˚C for 12 h. Cells were then washed with PBS three times to fully remove nonspecifically absorbed drug. The obtained sample was observed by CLSM.

2.5 Cytotoxicity of the SiNPs-DOX@RBCs

The standard colorimetric 3-(4,5-dimethylthiazol-2-yl)-2, 5-diphenyltetrazolium Bromide (MTT, Sigma-Aldrich, St. Louis, MO, USA) assay was carried out to determine the cell viabilities relative to SiNPs-DOX@RBC-treated U87MG cells. Briefly, U87MG cells were seeded into 96-well cell culture plates at 1×10^4 cells/well for 12 h. Thereafter, pure SiNPs-DOX, DOX, and SiNPs-DOX@RBCs with serial DOX dilutions (from 0.6 to 10 μg·mL^{-1}) were added to each experimental group and co-incubated with U87MG cells for 24 h. Next, 20 μL stock MTT (5 mg·mL^{-1}) was added to each well, and the cells were incubated for another 5 h at 37 ˚C.

The cells were lysed by 10% acidified sodium dodecyl sulfate (10% SDS), and cell viability was determined by measuring the absorbance at 570 nm with a microplate reader (Bio-Rad 680, Hercules, CA, USA). When 8×10^7 SiNPs-DOX@RBCs in 1 mL, SiNPs-DOX containing 5 μg·mL^{-1} DOX, and 5 μg·mL^{-1} free DOX aqueous solution were separately added to U87MG cells, corresponding tumor cell killing ability was observed. To ensure reproducibility, three independent experiments were performed and all measurements were carried out in triplicate.

2.6 Blood circulation time measurement *in vivo*

After encapsulating SiNPs-DOX into RBCs, at least three mice were intravenously injected with autologous SiNPs-DOX@RBCs (5×10^8 cells, 100 μL for each mouse). Approximately 5 μL of blood was extracted from the orbital sinus at different time points and then dispersed in 0.5 mL of PBS containing anticoagulants. Photoluminescence (PL) spectroscopy was applied to determine the concentration of SiNPs-DOX in the blood samples. The SiNPs-DOX level in blood was determined as the percentage of injected SiNPs-DOX amount per gram of blood (%ID·g^{-1} in blood). The error bars were based on at least three mice in each group.

3 Results and discussion

3.1 Characterization of SiNPs-DOX@RBCs

Figure 2(a) presents the transmission electronic microscopy (TEM) and high-resolution transmission electron microscopy (HRTEM) images of the SiNPs (Fig. 2(a1)) and SiNPs-DOX (Fig. 2(a2)), respectively, both of which appeared as spherical particles with similar sizes of ~ 3.1 and ~ 4.2 nm, respectively. Typically, the dynamic light scattering sizes of SiNPs and SiNPs-DOX were ~ 3.5 and ~ 4.6 nm, which were slightly larger than the TEM size (Fig. S1 in the ESM). These data provide additional confirmation of successful DOX loading onto SiNPs [41]. The resultant SiNPs-DOX were then encapsulated in RBCs to obtain SiNPs-DOX@RBCs, whose morphology remained nearly unchanged (typical biconcave shape similar to untreated RBCs) according to the scanning electron microscopy image in Fig. 2(a3), suggesting that membrane integrity was still maintained compared with natural RBCs (Fig. S2 in the ESM).

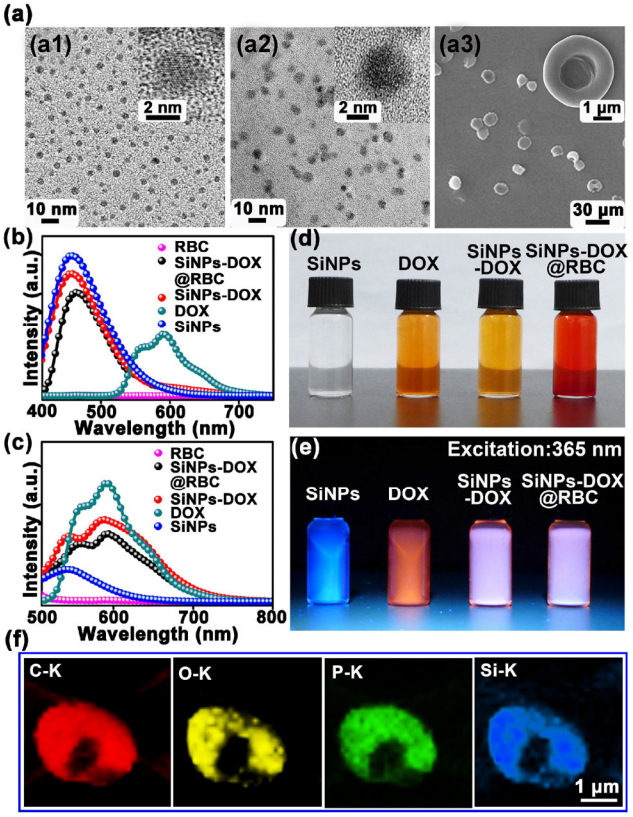

Figure 2 Characterization of SiNPs-DOX@RBCs. (a) TEM and HRTEM images of SiNPs (a1) and SiNPs-DOX (a2). Inset presents enlarged HRTEM images of SiNPs and SiNPs-DOX. Scanning electron microscopy and enlarged image of SiNPs-DOX@RBCs are shown in (a3). Fluorescence spectra of as-prepared samples excited by 405 (b) and 488 nm (c). Digital images of aqueous solution samples without (d) or with (e) UV irradiation. (f) Energy-dispersive X-ray mapping of the SiNPs-DOX@RBCs complex.

We further interrogated the optical properties of the SiNPs-DOX@RBCs. Specifically, the UV–vis absorption spectra indicated that both SiNPs-DOX@RBCs and pure SiNPs-DOX had two peaks at 320 and 490 nm (Fig. S3 in the ESM), which were ascribed to SiNPs and DOX, respectively. Moreover, the PL spectra are presented in Figs. 2(b) and 2(c). Under the excitation of 405 (Fig. 2(b)) or 488 nm (Fig. 2(c)) wavelengths, the PL spectra of SiNPs-DOX@RBCs and SiNPs-DOX both showed the characteristic PL peaks of SiNPs and DOX at λ_{max} of ~ 500 and ~ 600 nm, respectively, suggesting that RBCs are excellent drug carriers for SiNPs-DOX. As displayed in Figs. 2(d) and 2(e), all aqueous samples exhibited strong blue (SiNPs), red

(DOX), and pink (SiNPs-DOX and SiNPs-DOX@RBCs) fluorescence under UV irradiation. The estimated amount of DOX molecules in SiNPs-DOX complexes encapsulated in each RBC is shown in Fig. S4 in the ESM. The energy-dispersive X-ray mapping in Fig. 2(f) further demonstrated that in addition to common elements (e.g., C, O, and P) on the membrane of SiNPs-DOX@RBCs, distinct silicon element were detected (silicon is undetectable in natural RBCs, shown in Fig. S5 in the ESM).

Notably, obvious colocalization of SiNPs and DOX fluorescence was observed in the CLSM images of SiNPs-DOX@RBCs (Fig. 3(a)), indicating that SiNPs-DOX are encapsulated in RBCs. As presented in Fig. 3(a), for both the SiNPs- (Fig. 3(a1)) and DOX- (Fig. 3(a2)) channel, the fluorescence intensities were distinctly enhanced compared to untreated RBCs (Fig. S6 in the ESM). Flow cytometry data ensured that most RBCs after hypotonic hemolysis treatment contained SiNPs-DOX (Fig. 3(b)), which is consistent with the CLSM images. To further evaluate a single SiNPs-DOX@RBC, three-dimensional scanning was subsequently carried out as shown in Fig. 3(c). For simplicity, we defined the middle of the chosen RBC as 0 μm on the *z* axis. Images were acquired every 0.5 μm for a single SiNPs-DOX@RBC in z-stacks. The overall fluorescent signal consistently increased and reached a maximum when scanning the middle of a single SiNPs-DOX@RBC, suggesting that SiNPs-DOX were encapsulated inside RBCs. Obvious red fluorescence quenching was detected under high-power laser irradiation because of the relatively poor photostability of DOX. In contrast, the fluorescent signal from SiNPs was stable during the same imaging process. Furthermore, quantitative analysis of the PL intensity from SiNPs-DOX@RBCs was carried out as shown in Fig. 3(c). Both fluorescence signals from SiNPs and DOX increased during three-dimensional scanning, and the strongest signal in the middle of the chosen SiNPs-DOX@RBC is shown in Fig. 3(d). However, when z-stack scanning was performed at higher magnification (Fig. 3(c)), the concave centers of SiNPs-DOX@RBCs were not clearly discernible because of the limited resolution of our instrument. Moreover, to compare the photostability between DOX and SiNPs inside a single RBC, we determined the PL intensity ratio of the DOX and SiNPs at each scanning level (Fig. 3(e)). After 2-min high-power laser irradiation, the PL intensity of SiNPs remained strong and was approximately 30-fold higher than that of DOX because of the robust photostability of SiNPs and severe photobleaching of DOX molecules.

We examined additional properties of SiNPs-DOX@RBCs. Suspensions of natural RBCs and SiNPs-DOX@RBCs all showed favorable stability (Fig. S7(a) in the ESM). Notably, the cellular morphology of SiNPs-DOX@RBCs was maintained even after 7-day storage (Fig. S7(b) in the ESM). It is well-established that phosphatidylserine (PS) exposure is involved in the recognition and removal of damaged and senescent RBCs by the reticuloendothelial system [11]. Therefore, we evaluated PS exposure of SiNPs-DOX@RBCs in an

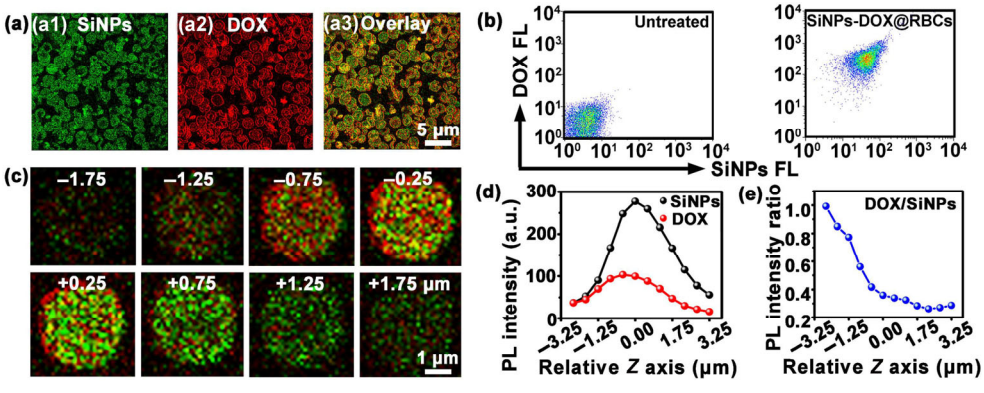

Figure 3 CLSM and flow cytometric analyses. (a) CLSM images of SiNPs-DOX@RBCs. (b) Flow cytometric analyses of natural RBCs and SiNPs-DOX@RBCs. (c) Scanning images from CLSM z-stacks (slice distance: 0.5 μm, time interval: 20 s) of a single SiNPs-DOX@RBC. PL intensity of SiNPs and DOX fluorescence from a single SiNPs-DOX@RBC (d), and their ratio corresponding to each scanning image (e).

Annexin V binding assay (Fig. S8 in the ESM), which revealed a PS exposure ratio of SiNPs-DOX@RBCs of 4.31%, a value much lower than that of RBCs ghost (87.9%). This result indicates that the method for SiNPs-DOX encapsulation does not cause significant damages to the membrane structure of RBCs. For the release behaviors in Fig. S9 in the ESM, the DOX released from SiNPs-DOX@RBCs was much slower than that of pure SiNPs-DOX (Fig. S9(b) in the ESM). In our system, SiNPs-DOX was released from RBCs by passive cross-membrane diffusion [42]. Next, DOX molecules were unloaded from SiNPs-DOX by pH-dependent release properties because of the higher solubility and improved hydrophilicity of DOX molecules in the acidic environments [34]. We consider that the release mechanism is that the SiNPs-DOX are stored and protected inside RBCs until released, preventing rapid excretion of SiNPs-DOX by renal clearance and improving the therapeutic effect *in vivo* [43].

3.2 Long-term and real-time tracking of SiNPs-DOX@RBCs *in vitro*

Because of the high photostability of SiNPs, SiNPs-DOX@RBCs are particularly suitable for long-term live cell tracking. Figure 4(a) shows CLSM images of a single U87MG cell treated with SiNPs-DOX@RBCs (containing 2.5 μg·mL^{-1} DOX) for 24 h. As shown in the images, DOX displayed spatially resolved fluorescence in the initial 3 min. However, the red fluorescence signal nearly disappeared after 10-min irradiation. In comparison, SiNPs showed remarkably stable fluorescence against photobleaching throughout the long-term imaging period, with the green signals remaining persistently strong during 25-min observation. The overlay channel clearly revealed the photobleaching evolution of the red signal, while the green signal of SiNPs remained stable during 25-min continuous observation by CLSM. For further comparison, quantitative calculation of the changes in PL intensities of SiNPs and DOX are presented in Fig. 4(b). The fluorescence of DOX quickly quenched in 10-min because of severe photobleaching (red); comparatively, SiNPs are extremely stable, maintaining ~ 76% of the initial intensity after 25 min of laser irradiation (black).

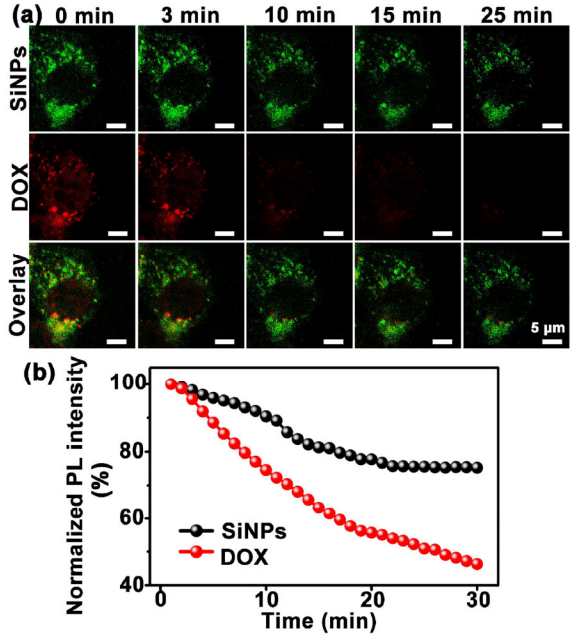

Figure 4 Fluorescence imaging of U87MG cells tracked by DOX and SiNPs during long-term irradiation. (a) Real-time fluorescence imaging of a single U87MG cell after incubation with SiNPs-DOX@RBCs for 24 h. (b) Quantitative analysis of changes in PL intensities of SiNPs (black) and DOX (red) inside a single U87MG cell during 30 min of imaging.

These data suggest the feasibility of these presented fluorescent drug nanocarriers for real-time and long-term live cell tracking.

3.3 Intracellular distribution, tumor cell killing ability *in vitro*, and half-life of the SiNPs-DOX@RBCs in blood

To gain further insight into the intracellular distribution of SiNPs-DOX@RBCs, the SiNPs-DOX@RBCs containing 2.5 μg·mL^{-1} DOX were incubated with U87MG cancer cells (Fig. 5(a), control groups are in Fig. S10 in the ESM). Compared to pure SiNPs-DOX, SiNPs-DOX released from RBCs showed a similar intracellular distribution, in which the fluorescence of SiNPs was mainly localized in the cytoplasm and DOX molecules were released and distributed in the nucleus. These data indicate that RBCs, as a type of high-performance DDS, can encapsulate drugs and release them without influencing their intracellular distribution.

Subsequently, we evaluated the potential of SiNPs-DOX@RBCs for cancer-cell destruction *in vitro* using

U87MG cells. A standard cell viability assay (Fig. 5(b)) and Calcein-AM/propidium iodide (PI) co-staining (Fig. S11 in the ESM) were carried out to evaluate treatment efficacy. DOX molecules are known to intercalate strongly into DNA and effectively destruct topoisomerase II enzyme [44]. When the cells were incubated with pure SiNPs-DOX and SiNPs-DOX@RBCs (see details in the supporting information), pure SiNPs-DOX led to a drastic decrease in cell viability (~ 63.3%) at a DOX concentrations at 5 μg·mL^{-1} (Fig. 5(b)). Similarly, the SiNPs-DOX@RBCs showed high cancer cell killing ability (56.8%) under the same experimental conditions. In addition, the cytotoxicity effect showed a clear positive correlation with DOX concentration (Fig. S12 in the ESM). These data collectively suggest that SiNPs-DOX@RBCs release DOX in a slow and sustained manner and have a highly effective cancer cell killing ability.

After demonstrating the excellent optical properties and effective tumor cell killing capability *in vitro*, we examined the SiNPs-DOX@RBCs blood circulation time *in vivo*. Previous studies showed that free DOX concentration rapidly decreases in the blood [45], while SiNPs-DOX have a relatively longer blood

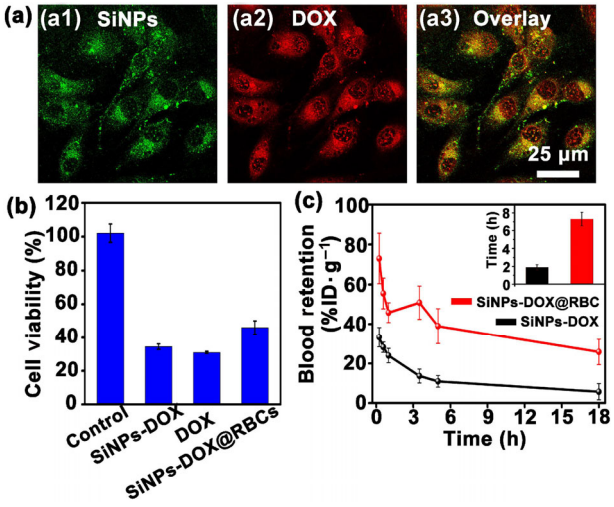

Figure 5 Tumor cell killing ability and half-life of SiNPs-DOX@RBCs in blood. (a) CLSM images of U87MG cells treated with SiNPs-DOX@RBCs. Fluorescence of SiNPs and DOX (released DOX and DOX retained on SiNPs) is defined as green and red, respectively. (b) *In vitro* cell viability of U87MG cells incubated with natural RBCs, pure SiNPs-DOX, free DOX and SiNPs-DOX@RBCs for 24 h. (c) Blood circulation data probed by the PL spectra for SiNPs-DOX@RBCs and SiNPs-DOX.

circulation time [34]. In our experiment, we systematically compared the blood circulation time of SiNPs-DOX and SiNPs-DOX@RBCs (Fig. 5(c)). Blood sampling revealed that SiNPs-DOX@RBCs had a much longer blood circulation time ($t_{1/2}$ = 7.31 ± 0.96 h) than pure SiNPs-DOX ($t_{1/2}$ = 1.90 ± 0.29 h). This pharmacokinetic result verifies that the resulting SiNPs-DOX@RBCs have a significantly extended blood circulation time, improving the accumulation of drugs in tumors. Notably, enhanced permeability and the retention (EPR) effect are widely recognized as dominant factors in the passive accumulation of NPs around tumors [46, 47]. In addition, recent studies revealed that the "NP-induced endothelial leakiness" (NanoEL) effect caused the formation of micrometer-sized gaps between endothelial cells because of the long-term interaction between NPs and the vasculature [48–52], leading to the SiNPs-DOX@RBCs exiting the vasculature and passively accumulating at tumor sites. Thus, the DDS can passively accumulate around tumors through the EPR and NanoEL effect.

4 Conclusions

In summary, we demonstrated that fluorescent SiNPs-DOX@RBCs simultaneously have favorable biocompatibility, excellent optical properties, and significantly lengthened blood residency. Specifically, compared to free DOX with rapid fluorescence quenching in 3 min, the SiNPs-DOX@RBC system maintained stable fluorescent intensity during 25-min high-power UV irradiation. Additionally, the blood circulation time of SiNPs-DOX@RBCs was 3.9-fold longer than that of pure SiNPs-DOX under optimal conditions. We demonstrated the feasibility of using SiNPs-DOX@RBCs for highly efficient chemotherapy in a long-term manner, showing potential for integrated diagnosis and therapy of cancers.

Acknowledgements

We express our grateful thanks to Prof. Shuit-Tong Lee for general help and valuable suggestion. We appreciate financial support from the National Basic Research Program of China (No. 2013CB934400), the National Natural Science Foundation of China (Nos.

61361160412 and 31400860), and a project funded by the Priority Academic Program Development of Jiangsu Higher Education Institutions (PAPD), 111 Project as well as Collaborative Innovation Center of Suzhou Nano Science and Technology (NANO-CIC).

Electronic Supplementary Material: Supplementary material (methods regarding preparation of SiNPs and SiNPs-DOX, data regarding TEM diameter and DLS measurement of SiNPs and SiNPs-DOX, SEM images of the SiNPs-DOX@RBCs, UV–vis absorbance spectra of the SiNPs-DOX and SiNPs-DOX@RBCs, quantification of DOX loading in the SiNPs-DOX@RBCs, scanning transmission electron microscopy and corresponding EDX mapping of a single natural RBC, CLSM images of natural RBCs, water dispersibility and storage stability of the SiNPs-DOX@RBCs, membrane integrity assessment of SiNPs-DOX@RBCs, release behavior of SiNPs-DOX from RBCs, *in vitro* drug delivery behavior of free DOX and pure SiNPs-DOX, Calcein AM & PI co-stained U87MG cells after incubation with DOX, SiNPs-DOX and SiNPs-DOX@RBCs, cytotoxicity of pure SiNPs-DOX, free DOX and SiNPs-DOX@RBCs treated U87MG cells) is available in the online version of this article at https://doi.org/10.1007/s12274-017-1850-6.

References

[1] Hong, G. S.; Diao, S.; Antaris, A. L.; Dai, H. J. Carbon nanomaterials for biological imaging and nanomedicinal therapy. *Chem. Rev.* **2015**, *115*, 10816–10906.

[2] Yan, J.; Hu, C. Y.; Wang, P.; Zhao, B.; Ouyang, X. Y.; Zhou, J.; Liu, R.; He, D. N.; Fan, C. H.; Song, S. P. Growth and origami folding of DNA on nanoparticles for high-efficiency molecular transport in cellular imaging and drug delivery. *Angew. Chem., Int. Ed.* **2015**, *54*, 2431–2435.

[3] Yoo, J.-W.; Irvine, D. J.; Discher, D. E.; Mitragotri, S. Bio-inspired, bioengineered and biomimetic drug delivery carriers. *Nat. Rev. Drug Discov.* **2011**, *10*, 521–535.

[4] Meyer, R. A.; Sunshine, J. C.; Green, J. J. Biomimetic particles as therapeutics. *Trends Biotechnol.* **2015**, *33*, 514–524.

[5] Tibbitt, M. W.; Dahlman, J. E.; Langer, R. Emerging frontiers in drug delivery. *J. Am. Chem. Soc.* **2016**, *138*, 704–717.

[6] Parodi, A.; Quattrocchi, N.; Van De Ven, A. L.; Chiappini, C.; Evangelopoulos, M.; Martinez, J. O.; Brown, B. S.; Khaled, S. Z.; Yazdi, I. K.; Enzo, M. V. et al. Synthetic nanoparticles functionalized with biomimetic leukocyte membranes possess cell-like functions. *Nat. Nanotechnol.* **2013**, *8*, 61–68.

[7] Fang, R. H.; Hu, C.-M. J.; Luk, B. T.; Gao, W. W.; Copp, J. A.; Tai, Y. Y.; O'Connor, D. E.; Zhang, L. F. Cancer cell membrane-coated nanoparticles for anticancer vaccination and drug delivery. *Nano Lett.* **2014**, *14*, 2181–2188.

[8] Gao, W. W.; Fang, R. H.; Thamphiwatana, S.; Luk, B. T.; Li, J. M.; Angsantikul, P. Z.; Zhang, Q. Z.; Hu, C.-M. J.; Zhang, L. F. Modulating antibacterial immunity via bacterial membrane-coated nanoparticles. *Nano Lett.* **2015**, *15*, 1403–1409.

[9] Hu, C.-M. J.; Fang, R. H.; Wang, K.-C.; Luk, B. T.; Thamphiwatana, S.; Dehaini, D.; Nguyen, P.; Angsantikul, P.; Wen, C. H.; Kroll, A. V. et al. Nanoparticle biointerfacing by platelet membrane cloaking. *Nature* **2015**, *526*, 118–121.

[10] Raemdonck, K.; Braeckmans, K.; Demeester, J.; De Smedt, S. C. Merging the best of both worlds: Hybrid lipid-enveloped matrix nanocomposites in drug delivery. *Chem. Soc. Rev.* **2014**, *43*, 444–472.

[11] Sun, X. Q.; Wang, C.; Gao, M.; Hu, A. Y.; Liu, Z. Remotely controlled red blood cell carriers for cancer targeting and near-infrared light-triggered drug release in combined photothermal-chemotherapy. *Adv. Funct. Mater.* **2015**, *25*, 2386–2394.

[12] Green, J. J.; Elisseeff, J. H. Mimicking biological functionality with polymers for biomedical applications. *Nature* **2016**, *540*, 386–394.

[13] Magnani, M.; Sfara, C.; Antonelli, A. Intravascular contrast agents in diagnostic applications: Use of red blood cells to improve the lifespan and efficacy of blood pool contrast agents. *Nano Res.* **2017**, *10*, 731–766.

[14] Shi, J.; Kundrat, L.; Pishesha, N.; Bilate, A.; Theile, C.; Maruyama, T.; Dougan, S. K.; Ploegh, H. L.; Lodish, H. F. Engineered red blood cells as carriers for systemic delivery of a wide array of functional probes. *Proc. Natl. Acad. Sci. USA* **2014**, *111*, 10131–10136.

[15] Peng, F.; Tu, Y. F.; van Hest, J. C. M.; Wilson, D. A. Self-guided supramolecular cargo-loaded nanomotors with chemotactic behavior towards cells. *Angew. Chem., Int. Ed.* **2015**, *54*, 11662–11665.

[16] Hu, C.-M. J.; Zhang, L.; Aryal, S.; Cheung, C.; Fang, R. H.; Zhang, L. Erythrocyte membrane-camouflaged polymeric nanoparticles as a biomimetic delivery platform. *Proc. Natl. Acad. Sci. USA* **2011**, *108*, 10980–10985.

[17] Luk, B. T.; Fang, R. H.; Hu, C.-M. J.; Copp, J. A.; Thamphiwatana, S.; Dehaini, D.; Gao, W. W.; Zhang, K.; Li, S. L.; Zhang, L. F. Safe and immunocompatible nanocarriers cloaked in RBC membranes for drug delivery to treat solid tumors. *Theranostics* **2016**, *6*, 1004–1011.

[18] Fu, Q.; Lv, P. P.; Chen, Z. K.; Ni, D. Z.; Zhang, L. J.; Yue, H.; Yue, Z. G.; Wei, W.; Ma, G. H. Programmed co-delivery of paclitaxel and doxorubicin boosted by camouflaging with erythrocyte membrane. *Nanoscale* **2015**, *7*, 4020–4030.

[19] Zhou, J.; Yang, Y.; Zhang, C.-Y. Toward biocompatible semiconductor quantum dots: From biosynthesis and bioconjugation to biomedical application. *Chem. Rev.* **2015**, *115*, 11669–11717.

[20] Blanco, E.; Shen, H. F.; Ferrari, M. Principles of nanoparticle design for overcoming biological barriers to drug delivery. *Nat. Biotechnol.* **2015**, *33*, 941–951.

[21] Wu, Z. G.; de Ávila, B. E.-F.; Martín, A.; Christianson, C.; Gao, W. W.; Thamphiwatana, S. K.; Escarpa, A.; He, Q.; Zhang, L. F.; Wang, J. RBC micromotors carrying multiple cargos towards potential theranostic applications. *Nanoscale* **2015**, *7*, 13680–13686.

[22] Dehaini, D.; Wei, X. L.; Fang, R. H.; Masson, S.; Angsantikul, P.; Luk, B. T.; Zhang, Y.; Ying, M.; Jiang, Y.; Kroll, A. V. et al. Erythrocyte-platelet hybrid membrane coating for enhanced nanoparticle functionalization. *Adv. Mater.* **2017**, *29*, 1606209.

[23] Howes, P. D.; Chandrawati, R.; Stevens, M. M. Colloidal nanoparticles as advanced biological sensors. *Science* **2014**, *346*, 1247390.

[24] Qing, Q.; Jiang, Z.; Xu, L.; Gao, R. X.; Mai, L. Q.; Lieber, C. M. Free-standing kinked nanowire transistor probes for targeted intracellular recording in three dimensions. *Nat. Nanotechnol.* **2014**, *9*, 142–147.

[25] Cheng, X. Y.; Lowe, S. B.; Reece, P. J.; Gooding, J. J. Colloidal silicon quantum dots: From preparation to the modification of self-assembled monolayers (SAMs) for bio-applications. *Chem. Soc. Rev.* **2014**, *43*, 2680–2700.

[26] Yu, T.; Wang, F.; Xu, Y.; Ma, L. L.; Pi, X. D.; Yang, D. R. Graphene coupled with silicon quantum dots for high-performance bulk-silicon-based Schottky-Junction photodetectors. *Adv. Mater.* **2016**, *28*, 4912–4919.

[27] Kim, D.; Zuidema, J. M.; Kang, J.; Pan, Y. L.; Wu, L. B.; Warther, D.; Arkles, B.; Sailor, M. J. Facile surface modification of hydroxylated silicon nanostructures using heterocyclic silanes. *J. Am. Chem. Soc.* **2016**, *138*, 15106–15109.

[28] McVey, B. F. P.; Tilley, R. D. Solution synthesis, optical properties, and bioimaging applications of silicon nanocrystals. *Acc. Chem. Res.* **2014**, *47*, 3045–3051.

[29] Peng, F.; Su, Y. Y.; Zhong, Y. L.; Fan, C. H.; Lee, S.-T.; He, Y. Silicon nanomaterials platform for bioimaging, biosensing, and cancer therapy. *Acc. Chem. Res.* **2014**, *47*, 612–623.

[30] Montalti, M.; Cantelli, A.; Battistelli, G. Nanodiamonds and silicon quantum dots: Ultrastable and biocompatible luminescent nanoprobes for long-term bioimaging. *Chem. Soc. Rev.* **2015**, *44*, 4853–4921.

[31] Pang, J. Y.; Su, Y. Y.; Zhong, Y. L.; Peng, F.; Song, B.; He, Y. Fluorescent silicon nanoparticle-based gene carriers featuring strong photostability and feeble cytotoxicity. *Nano Res.* **2016**, *9*, 3027–3037.

[32] Zhong, Y. L.; Peng, F.; Bao, F.; Wang, S. Y.; Ji, X. Y.; Yang, L.; Su, Y. Y.; Lee, S.-T.; He, Y. Large-scale aqueous synthesis of fluorescent and biocompatible silicon nanoparticles and their use as highly photostable biological probes. *J. Am. Chem. Soc.* **2013**, *135*, 8350–8356.

[33] Li, Q.; Luo, T.-Y.; Zhou, M.; Abroshan, H.; Huang, J. C.; Kim, H. J.; Rosi, N. L.; Shao, Z. Z.; Jin, R. C. Silicon nanoparticles with surface nitrogen: 90% quantum yield with narrow luminescence bandwidth and the ligand structure based energy law. *ACS Nano* **2016**, *10*, 8385–8393.

[34] Ji, X. Y.; Peng, F.; Zhong, Y. L.; Su, Y. Y.; Jiang, X. X.; Song, C. X.; Yang, L.; Chu, B. B.; Lee, S.-T.; He, Y. Highly fluorescent, photostable, and ultrasmall silicon drug nanocarriers for long-term tumor cell tracking and *in-vivo* cancer therapy. *Adv. Mater.* **2015**, *27*, 1029–1034.

[35] Petros, R. A.; DeSimone, J. M. Strategies in the design of nanoparticles for therapeutic applications. *Nat. Rev. Drug Discov.* **2010**, *9*, 615–627.

[36] Vallet-Regí, M.; Balas, F.; Arcos, D. Mesoporous materials for drug delivery. *Angew. Chem., Int. Ed.* **2007**, *46*, 7548–7558.

[37] Peng, F.; Su, Y. Y.; Wei, X.; Lu, Y. P.; Zhou, Y. F.; Zhong, Y. L.; Lee, S.-T.; He, Y. Silicon-nanowire-based nanocarriers with ultrahigh drug-loading capacity for *in vitro* and *in vivo* cancer therapy. *Angew. Chem., Int. Ed.* **2013**, *52*, 1457–1461.

[38] Kolesnikova, T. A.; Skirtach, A. G.; Möhwald, H. Red blood cells and polyelectrolyte multilayer capsules: Natural carriers versus polymer-based drug delivery vehicles. *Exp. Opin. Drug Deliv.* **2013**, *10*, 47–58.

[39] Wang, C.; Sun, X. Q.; Cheng, L.; Yin, S. N.; Yang, G. B.; Li, Y. G.; Liu, Z. Multifunctional theranostic red blood cells for magnetic-field-enhanced *in vivo* combination therapy of cancer. *Adv. Mater.* **2014**, *26*, 4794–4802.

[40] Purow, B.; Schiff, D. Advances in the genetics of glioblastoma: Are we reaching critical mass? *Nat. Rev. Neurol.* **2009**, *5*, 419–426.

[41] Zhong, Y. L.; Peng, F.; Wei, X. P.; Zhou, Y. F.; Wang, J.; Jiang, X. X.; Su, Y. Y.; Su, S.; Lee, S. T.; He, Y. Microwave-assisted synthesis of biofunctional and fluorescent silicon nanoparticles using proteins as hydrophilic ligands. *Angew. Chem., Int. Ed.* **2012**, *51*, 8485–8489.

[42] Luk, B. T.; Zhang, L. F. Cell membrane-camouflaged nanoparticles for drug delivery. *J. Control. Release* **2015**, *220*, 600–607.

[43] Li, B. L.; Setyawati, M. I.; Chen, L. Y.; Xie, J. P.; Ariga, K.; Lim, C.-T.; Garaj, S.; Leong, D. T. Directing assembly and disassembly of 2D MoS_2 nanosheets with DNA for drug delivery. *ACS Appl. Mater. Interfaces* **2017**, *9*, 15286–15296.

[44] Rim, H. P.; Min, K. H.; Lee, H. J.; Jeong, S. Y.; Lee, S. C. pH-tunable calcium phosphate covered mesoporous silica nanocontainers for intracellular controlled release of guest drugs. *Angew. Chem., Int. Ed.* **2011**, *50*, 8853–8857.

[45] Minchinton, A. I.; Tannock, I. F. Drug penetration in solid tumours. *Nat. Rev. Cancer* **2006**, *6*, 583–592.

[46] Ren, X. Q.; Zheng, R.; Fang, X. L.; Wang, X. F.; Zhang, X. Y.; Yang, W. L.; Sha, X. Y. Red blood cell membrane camouflaged magnetic nanoclusters for imaging-guided photothermal therapy. *Biomaterials* **2016**, *92*, 13–24.

[47] Su, J. H.; Sun, H. P.; Meng, Q. S.; Yin, Q.; Tang, S.; Zhang, P. C.; Chen, Y.; Zhang, Z. W.; Yu, H. J.; Li, Y. P. Long circulation red-blood-cell-mimetic nanoparticles with peptide-enhanced tumor penetration for simultaneously inhibiting growth and lung metastasis of breast cancer. *Adv. Funct. Mater.* **2016**, *26*, 1243–1252.

[48] Setyawati, M. I.; Tay, C. Y.; Docter, D.; Stauber, R. H.; Leong, D. T. Understanding and exploiting nanoparticles' intimacy with the blood vessel and blood. *Chem. Soc. Rev.* **2015**, *44*, 8174–8199.

[49] Setyawati, M. I.; Tay, C. Y.; Chia, S. L.; Goh, S. L.; Fang, W.; Neo, M. J.; Chong, H. C.; Tan, S. M.; Loo, S. C.; Ng, K. W. et al. Titanium dioxide nanomaterials cause endothelial cell leakiness by disrupting the homophilic interaction of VE-cadherin. *Nat. Commun.* **2013**, *4*, 1673.

[50] Setyawati, M. I.; Mochalin, V. N.; Leong, D. T. Tuning endothelial permeability with functionalized nanodiamonds. *ACS Nano* **2016**, *10*, 1170–1181.

[51] Tay, C. Y.; Setyawati, M. I.; Leong, D. T. Nanoparticle density: A critical biophysical regulator of endothelial permeability. *ACS Nano* **2017**, *11*, 2764–2772.

[52] Setyawati, M. I.; Tay, C. Y.; Bay, B. H.; Leong, D. T. Gold nanoparticles induced endothelial leakiness depends on particle size and endothelial cell origin. *ACS Nano* **2017**, *11*, 5020–5030.